JGR Biogeosciences

RESEARCH ARTICLE
10.1029/2019JG005203

Special Section:
Quantifying Nutrient Budgets for sustainable nutrient management

Projections of Atmospheric Nitrogen Deposition to the Chesapeake Bay Watershed

Patrick C. Campbell[1,2,3], Jesse O. Bash[4], Christopher G. Nolte[4], Tanya L. Spero[4], Ellen J. Cooter[4], Kyle Hinson[5,6], and Lewis C. Linker[7]

[1]National Academies/National Research Council (NRC) Fellowship Participant, U.S. Environmental Protection Agency, Research Triangle Park, NC, USA, [2]Now at Center for Spatial Information Science and Systems, George Mason University, Cooperative Institute for Satellite Earth System Studies, Fairfax, MD, USA, [3]ARL/NOAA Affiliate, Silver Spring, MD, USA, [4]National Exposure Research Laboratory, U.S. Environmental Protection Agency, Durham, NC, USA, [5]Chesapeake Bay Research Consortium, Edgewater, MD, USA, [6]Now at Virginia Institute of Marine Science, Gloucester Point, VA, USA, [7]U.S. Environmental Protection Agency, Chesapeake Bay Program Office, Annapolis, MD, USA

Abstract Atmospheric deposition is among the largest pathways of nitrogen loading to the Chesapeake Bay Watershed (CBW). The interplay between future climate and emission changes in and around the CBW will likely shift the future nutrient deposition abundance and chemical regime (e.g., oxidized vs. reduced nitrogen). In this work, a Representative Concentration Pathway from the Community Earth System Model is dynamically downscaled using a recently updated Weather Research and Forecasting model that subsequently drives the Community Multiscale Air Quality model coupled to the agroeconomic Environmental Policy Integrated Climate model. The relative impacts of emission and climate changes on atmospheric nutrient deposition are explored for a recent historical period and a period centered on 2050. The projected regional emissions in Community Multiscale Air Quality reflect current federal and state regulations, which use baseline and projected emission years 2011 and 2040, respectively. The historical simulations of 2-m temperature (T2) and precipitation (PRECIP) have cool and dry biases, and temperature and PRECIP are projected to both increase. Ammonium wet deposition agrees well with observations, but nitrate wet deposition is underpredicted. Climate and deposition changes increase simulated future ammonium fertilizer application. In the CBW by 2050, these changes (along with widespread decreases in anthropogenic nitrogen oxide and sulfur oxide emissions, and relatively constant ammonia emissions) decrease total nitrogen deposition by 21%, decrease annual average oxidized nitrogen deposition by 44%, and increase reduced nitrogen deposition by 10%. These results emphasize the importance of decreased anthropogenic emissions on the control of future nitrogen loading to the Chesapeake Bay in a changing climate.

Plain Language Summary In this study a global climate scenario is used to drive a regional-scale weather and air quality model to investigate the potential impacts of future climate and emission changes on atmospheric nitrogen loading to the Chesapeake Bay Watershed (CBW). While different scenarios are possible, here we delve into a specific climate projection that represents a future pathway for stabilization of radiative forcing by the year 2050 and use projected emissions (from human activity) that are based on historical and proposed regulations and controls from the U.S. Environmental Protection Agency. The combined climate and emission changes lead to decreases in the atmospheric nitrogen loading to the Chesapeake Bay Watershed by the year 2050, while the effects of climate alone lead to a small increase in atmospheric nitrogen loading. The results demonstrate the importance of emission reductions on nitrogen loading to the Chesapeake Bay, in the face of climate change.

Key Points:
- Combined climate and emission changes lead to reduced nitrogen deposition (~21%) to the Chesapeake Bay Watershed by 2050
- There is an offset in nitrogen deposition (approximately +4%) due to the change in climate by 2050
- The composition of the nitrogen deposition is becoming increasingly dominated by reduced nitrogen by 2050

Supporting Information:
- Supporting Information S1

Correspondence to:
P. C. Campbell,
patrick.c.campbell@noaa.gov

Citation:
Campbell, P. C., Bash, J. O., Nolte, C. G., Spero, T. L., Cooter, E. J., Hinson, K., & Linker, L. C. (2019). Projections of Atmospheric Nitrogen Deposition to the Chesapeake Bay Watershed. *Journal of Geophysical Research: Biogeosciences*, *124*, 3307–3326. https://doi.org/10.1029/2019JG005203

Received 10 APR 2019
Accepted 7 OCT 2019
Accepted article online 24 OCT 2019
Published online 7 NOV 2019

Published 2019. This article is a U.S. Government work and is in the public domain in the USA.

1. Introduction

The CBW is home to over 18 million people, and it provides over $100 billion in total economic benefits annually (Chesapeake Bay Foundation, 2014). The growth in industry, population, and agriculture in the CBW has degraded water quality and living resources in the Chesapeake Bay (EPA, 2010). The decline in living resources is largely attributed to hypoxia from excessive nutrient loading (Linker, Batiuk, et al., 2013). In 2010, the Chesapeake Bay Total Maximum Daily Load was established to reduce the nutrient loading to the CBW and improve the living and recreational uses of the bay (EPA, 2010). Atmospheric deposition of nitrogen (N) through scavenging by PRECIP (i.e., wet deposition) or the loss of nitrogen-containing gases and

particles to the surface (i.e., dry deposition (DD)) is among the largest sources of N to the CBW (Eschleman & Sabo, 2016; Linker, Dennis, et al., 2013). Reductions in total atmospheric N deposition in the United States through regulations promulgated under the Clean Air Act, and recent shifts from coal to natural gas to fuel electrical generation have been well documented (De Gouw et al., 2014). However, the recent changes in emissions have not been uniformed for all N-containing atmospheric pollutants. Regulations and shifts in energy production have decreased oxidized N emissions (NO_x) from combustion sources, while emissions of reduced N ($NH_x = NH_3$ + ammonium [NH_4^+]), primarily from agricultural and livestock sources, have remained relatively constant (Li, Schichtel, et al., 2016). This shift in emissions alters the atmospheric particulate matter formation that cascades through the transport and fate of atmospheric N.

The climate system is warming, and many of the observed changes since the 1950s are unprecedented over decades to millennia (IPCC, 2014). There is also medium to high confidence that continued emission of greenhouse gases (GHGs) will enhance warming, resulting in long-lasting changes in all components of the climate system (IPCC, 2014). Hence the climate trends have not been static in and around the Chesapeake Bay (Chesapeake Bay Foundation, 2007), and the associated changes in temperature, PRECIP, and sea level can act as stressors on the flora and fauna that help to maintain good water quality in the CBW while compromising environmental integrity. Hypoxia in coastal systems is sensitive to changes in patterns of temperature, PRECIP delivery, and wind-driven mixing as well as nutrient loading (Li, Lee, et al., 2016). Wind direction and speed, cloud cover, and sea surface temperature can also influence the development of hypoxia (Breitburg et al., 2018; Scully, 2010), which can further influence the fate and transport of atmospheric pollutants. To date, the individual and combined impacts of climate and emissions changes on the N loading of NH_x and NO_x to the CBW have not been well assessed.

This study focuses on N emissions in the Chesapeake Bay's airshed, the deposition of N to the CBW, and ways in which the loading of N could change in response to emission changes and potential climate and agroecosystem changes. Emitted N species, including both NO_x emissions and NH_3 emissions, are examined in detail as they relate to deposition. NO_x emissions have decreased in the United States nationally by nearly 41% from 1990 to 2010 (https://www.epa.gov/air-emissions-inventories/air-pollutant-emissions-trends-data); are dominated by the onroad, nonroad, and nonpoint (e.g., ship, rail, and aircraft) sources in the 2011 National Emissions Inventory (NEI); and are projected to further decline due to the increased fuel efficiency and tighter standards that are proposed to continue in the coming decades (EPA, 2016a, 2016b). Meanwhile, NH_3 emissions are relatively unregulated and have increased by 11% from 1990 to 2010 (Li, Schichtel, et al., 2016). There is greater uncertainty in the characterization of agricultural sector NH_3 emissions in the 2011NEI platform compared to NO_x sources, due to fewer in situ observations and emissions monitoring data than exist for NO_x (Nowak et al., 2012; Paulot et al., 2014; Walker et al., 2012; Zhu et al., 2013). Here the relative impacts of climate and emissions trends on the loading of N to the CBW are assessed with a focus on the projected changes to total N deposition, composed primarily of NH_x and NO_x to these loads. Text S1 in the Supplementary Information provides a list of commonly used acronyms and abbreviations found in this section and throughout the remainder of the paper.

2. Model Details and Design

2.1. Model Setup

To probe the impacts of changing climate and emissions on atmospheric N deposition from a global to regional scale, we use data from the Community Earth System Model (CESM) Version 1.0 over a global domain at horizontal resolution of 0.9° × 1.25°. For this study the CESM is driven by a Representative Concentration Pathway (RCP) scenario (van Vuuren et al., 2011) that assumes stabilized anthropogenic radiative forcing at 4.5 W/m^2 (RCP4.5) by the year 2100 (Thomson et al., 2011). Global climate output from CESM is not sufficient to support the regional air quality and deposition analyses in this work, and thus the output is dynamically downscaled using the Weather Research and Forecasting (WRF) model Version 3.8.1 (Powers et al., 2017; Skamarock & Klemp, 2008). WRF is then run continuously (no reinitialization) for historical (HIST: 1995–2004) and future (FUT: 2045–2054) decadal periods over a domain centered on the contiguous United States (CONUS) at a horizontal grid spacing of 36 km with 35 vertical levels from the surface to 50 hPa (see Figure S1 for the domain map and configuration details used in this study). The WRF simulations use higher-resolution topography, land/water interfaces, land use/land cover data, and robust physical

parameterizations to project changes to surface, atmospheric, and radiation fields. Additional details on the downscaling methodology and analysis are provided elsewhere (Nolte et al., 2018; Spero et al., 2016). The downscaled WRF fields are then processed using the Meteorology-Chemistry Interface Processor Version 4.3 (Otte & Pleim, 2010) for input into the Community Multiscale Air Quality (CMAQ) model (Byun & Schere, 2006) Version 5.2 (EPA, 2017) to simulate time-varying emissions, dynamic air-surface exchange of trace gases and aerosols, gas-phase chemistry, secondary aerosol formation, transport, and deposition for the HIST and FUT periods.

2.2. Model Configuration and Inputs

2.2.1. Configuration

A modified WRFv3.8.1-CMAQv5.2 system (hereafter referred to as WRF-CMAQ) is used, which has an improved linkage between the WRF/Noah land surface model and DD processes modeled by CMAQ (Campbell et al., 2019). The physical/chemical model configuration is the same here as in Campbell et al. (2019), where the CMAQ configuration includes the Carbon Bond 2005 gas phase mechanism with updates for toluene and chlorine chemistry (CB05TUCL; Sarwar et al., 2011) and the AERO6 aerosol module with semivolatile primary and secondary organic carbon (Appel et al., 2013; Nolte et al., 2015; Simon & Bhave, 2012).

The model inputs in this study differs from Campbell et al. (2019) in the nudging, land use data, meteorological and chemical initial and boundary conditions, anthropogenic emissions, dynamic greenhouse gas (GHG) mixing ratios in the downscaled WRF simulations, and agroecosystem inputs for the bidirectional ammonia (NH_3) flux model (BIDI-NH_3) in CMAQ. Here the 24-category U.S. Geological Survey land use/land cover classification system is used in WRF, which was augmented so that lakes are distinguished by an extra category as in Spero et al. (2016).

2.2.2. Downscaling and Boundary Conditions

WRF is used to dynamically downscale CESM, and it includes an updated treatment of inland water bodies following Spero et al. (2016). In this case, WRF also uses spectral nudging above the PBL of wavelengths >1,500 km from CESM. The chemical initial and boundary conditions for both CMAQ simulation periods originate from a simulation of 2011 using the GEOS-Chem global chemical transport model (Bey et al., 2001; Henderson et al., 2014; Lam & Fu, 2009), which is the same as in Nolte et al. (2018). The general approaches used for similar downscaling with WRF and CMAQ have been well documented; however, there are some downscaling nuances that differ across applications (e.g., Gao et al., 2013; Nolte et al., 2008; Nolte et al., 2018; Otte et al., 2012; Weaver et al., 2009).

To improve consistency between CESM and WRF, annual GHG values from the RCP4.5 scenario (IPCC, 2014) are used in the WRF radiation module. This method ensures that carbon dioxide (CO_2), nitrous oxide (N_2O), methane (CH_4), and chlorofluorocarbons 11 (CFC11) and 12 (CFC12) can evolve in both the HIST and FUT period. Further, the static background CO_2 and CH_4 mixing ratios were modified in CMAQ to be consistent with WRF. The HIST and FUT constant CO_2 (CH_4) values used in CMAQ are 368 ppm (1.743 ppm) and 485 ppm (1.833 ppm), respectively. This enables WRF-CMAQ to respond to both direct (e.g., CMAQ CH_4 oxidation pathways) and indirect (e.g., WRF temperature and rates of reactions) impacts from changing GHGs under HIST and projected FUT conditions, which better align with the CESM simulation.

2.2.3. Historical and Future Emissions

The HIST period anthropogenic emissions are from the U.S. Environmental Protection Agency (EPA) 2011v6.2 modeling platform (EPA, 2015) and are based on the 2011 NEI Version 2 (hereafter referred to as 2011NEI; EPA, 2016a; http://www.epa.gov/ttn/chief/net/2011inventory.html#inventorydoc). The major 2011NEI categories (sectors) incorporated in this work include (1) point (Electric Generating Units (EGUs), non-EGUs, and point oil and gas), (2) nonpoint (agricultural, agricultural fires, fugitive dust, rail, commercial marine, nonpoint oil and gas, and residential wood combustion), (3) nonroad, (4) onroad, (5) point source fires, and (6) other sources in Canada and Mexico (other fugitive dust, point, nonpoint and nonroad, and onroad). The primary emissions modeling tool used to create the air quality model-ready emissions for CMAQ was the Sparse Matrix Operator Kernel Emissions program (http://www.smoke-model.org), Version 3.6.5, which includes a number of different integrated model programs within (e.g., Sparse Matrix Operator Kernel Emissions-Motor Vehicle Emissions Simulator (MOVES) for the onroad sector), while incorporating gridded meteorological data from WRF Version 3.4 model simulations that are

Table 1
National CAPs emissions summary data values based on section 5, Tables 5-1 and 5-2 in EPA (2016a)

	NO_x	NH_3	CO	SO_2	AVOC	PM_{10}	$PM_{2.5}$
CONUS emission totals (Mt/yr)							
2011NEI	14.21	4.18	71.43	6.39	17.31	11.26	4.59
2040ref	6.96	4.26	51.30	2.19	14.88	12.64	4.47
% change	−51.07	1.97	−28.17	−65.77	−14.08	12.23	−2.51
Non-CONUS emission totals (Mt/yr)							
2011NEI	2.78	0.53	10.53	1.35	2.07	1.23	0.42
2040ref	2.64	0.55	9.32	1.11	2.13	1.24	0.43
% change	−5.07	3.10	−11.44	−17.79	3.04	1.31	1.76

Note. The relative (%) change is defined as [(2040ref/2011NEI)−1] × 100%, and the text is colored red for increases and blue for decreases.

consistent with the Air Quality Modeling Technical Support Document used in the rulemaking (EPA, 2016b). Details regarding development of 2011NEI model-ready emissions for each category and applicable subsectors are well described in EPA (2016a), including detailed descriptions of certain key differences between a relatively updated 2011v6.2 modeling platform compared to the base 2011NEI (also summarized here in the Supporting Information).

Particularly relevant to this work, the agricultural NH_3 sector emissions dominate (>80%) the total anthropogenic NH_3 emission load (Reis et al., 2009), while past shifts in decreasing NO_x and increasing NH_3 emissions have led to an increased importance of atmospheric NH_x deposition in the United States (Li, Schichtel, et al., 2016). Thus, we briefly summarize the details for the agriculture NH_3 sector developed in the 2011NEI, as the details are important for interpreting the CONUS NH_3 emission changes shown below, and their impacts on future N changes in the CBW. The 2011NEI agriculture NH_3 sector includes both livestock NH_3 sources and all the NH_3 emissions from agricultural fertilization in the 2011NEI. Livestock sources include beef cattle, poultry production and waste emissions, dairy cattle, cattle and calves waste emissions, swine production, horses and ponies waste emissions, sheep and lambs waste emissions, and goats waste emissions. The agriculture NH_3 sector does not include all the livestock NH_3 emissions, as a small amount of NH_3 emissions is included within the livestock feedlots source in the non-EGU point sector for California and Wisconsin (EPA, 2016a). As an agroecosystem model (described below) is coupled to the CMAQ BIDI-NH_3 model in this work (BIDI-NH_3 exchange estimates emissions from fertilizer application in-line), the NH_3 emissions from agriculture fertilizer applications to crops are removed from the emissions inventory to avoid double counting of this source (Bash et al., 2013).

The FUT period emissions are part of a joint rulemaking effort under the Clean Air Act and the Energy Independence and Security Act of 2007 and are based on federal and state regulations and measures for the year 2040 reference (2040ref) case, which had been promulgated by August 2015 (EPA, 2016a). They represent the impact of current "on-the-books" regulations without implementation of the Heavy-Duty Vehicle Greenhouse Gas Phase 2 rule (EPA, 2016a). The future period emissions for the 2040ref case are created by using different projection methods (e.g., running models or using best estimates) that are specific to the sources in the various sectors, while some sectors/sources remain the same in both the historical and future. Hence, there is a significant amount of detail within each source/sector projection, which may be found in section 4 of EPA (2016a) and is not repeated here; however, important to the discussion below and in later sections, we briefly summarize the major aspect of each sector's projection methods (if applicable) and the list of criteria air pollutants (CAPs) (NH_3, carbon monoxide [CO], NO_x, sulfur dioxide [SO_2], volatile organic compounds [VOC], and particulate matter with an aerodynamic diameter <10 μm [PM_{10}] and <2.5 μm [$PM_{2.5}$]) impacted in Table S1. We note that some emission sectors/sources in the 2040ref case are not projected to the year 2040 and are representative of earlier periods (Table S1). Biogenic emissions are not included in either the 2011NEI or 2040ref emission files. Rather they are calculated in CMAQ using the Biogenic Emissions Inventory System Version 3.6 and are dependent on the climate/meteorology (e.g., temperature and insolation) of the period. Thus, the pertinent biogenic VOC species are projected in the FUT periods, as these CMAQ runs incorporate the future years' meteorological conditions.

Table 1 summarizes the total emissions differences between the 2011NEI and 2040ref case for the CAPs (based on data in EPA, 2016a) and shows that there are CONUS decreases in NO_x (51%), CO (28%), SO_2 (66%), and anthropogenic VOC (AVOC) (14%) emissions in the 2040ref projections compared to 2011NEI. The decreases in NO_x, CO, and AVOC are driven by nationally modeled onroad and nonroad sector rules, which included more stringent vehicle emissions and fuel standards (e.g., Tier 3 and Tier 4 Vehicle Emissions and Fuel Standards Program) in the future. The large decreases in SO_2 2040ref emissions in the United States are strongly driven by future state rules, consent decrees, and announced shutdowns of point EGUs that are modeled to future years (Table S1) (EPA, 2016a). The SO_2 emission decreases are also strongly impacted by the implementation of several national regulations, including those aimed at reducing both

pollutants and GHGs in the future. The decreases in NO_x and CO in the non-CONUS regions are dominated by onroad emission decreases in Mexico, while the decreases in SO_2 in the non-CONUS are driven by point EGUs in Mexico, offshore, and commercial marine vessels. The larger increases in PM_{10} emissions in CONUS (12%) are strongly driven by increases in fugitive dust from Annual Energy Outlook-based Vehicle Miles Travelled (VMT) growth for paved and unpaved roads. While there are also increases in $PM_{2.5}$ from fugitive dust, the larger decreases in emissions from onroad and nonroad sectors lead to a slight CONUS average decrease for $PM_{2.5}$ (3%).

NH_3 emissions are relatively unregulated compared to the other CAPs above, and there are small increases across the CONUS (2%) and non-CONUS regions (3%) (Table 1). The increases in NH_3 emissions are driven by agricultural livestock emissions growth from the year 2011 to 2030 (Table S1), and there is no projection of future NH_3 from fertilizer application in the 2040ref emissions for CONUS. The changes in NH_3 fertilizer emissions in CONUS are driven by the coupled Environmental Policy Integrated Climate (EPIC) and CMAQ BIDI-NH_3 exchange model framework. Figure 1 shows a spatial comparison of NO_x and NH_3 2011NEI emissions used in CMAQ, as well as their absolute and relative changes (2040ref – 2011NEI) in the Chesapeake Bay Airshed (CBA). Figure S2 also shows domain-wide absolute spatial emission difference plots for NO_x, NH_3, and the other CAPs, while Figure S3 shows the NO_x and NH_3 emission changes in the CBW for comparison.

There are widespread decreases in NO_x emissions across CONUS, especially in the eastern United States and in the CBA. Maximum decreases are in urban regions that experience a significant decrease in future onroad NO_x emissions. There are also widespread increases in NH_3 emissions across the CONUS due to increased agricultural NH_3 emissions, while the decreases in parts of the western United States including California are due to decreases in large onroad emission sources. The larger relative change in NO_x and NH_3 emissions off the East and West Coast of CONUS is due to commercial marine vehicle (i.e., ship) emission changes that are large relative to small emission magnitudes in these regions. The average relative changes in NO_x and NH_3 emissions in the CBA (CBW) are about −55% (−60%) and +7% (−0.4%), respectively. There are also widespread decreases in CO, SO_2, and AVOC emissions, with some localized increases in SO_2 and AVOC emissions, as well as widespread increases in PM_{10} and $PM_{2.5}$ emissions (except in a few states including California) across the eastern United States (Figure S2) and the CBA (Figure 1).

It is worth noting that the 2011NEI NH_3 emissions used in these simulations are estimated using the same methods as they are in the 2014NEI, while the NO_x emissions in the 2014NEI are 13% lower than the 2011NEI, as shown in Table 2.6 in the 2014v2 NEI Technical Support Document (EPA, 2018). The bulk of the NO_x reduction in the 2014NEI is due to mobile sources and would certainly have an impact in the projected NO_x deposition to the bay, as would any potential repeals of the NO_x rules set forth in the EPA (2016a) final rule. In this study, WRF-CMAQ is linked to agricultural cropping management and soil biogeochemical processes in the agroecosystem Environmental Policy Integrated Climate (EPIC) model (Cooter et al., 2012) to improve simulated changes to N deposition over the CBW. The EPIC model uses weather- and climate-dependent soil conditions to calculate fertilizer application timing, rate, depth and composition that are used in BIDI-NH_3 flux modeling in CMAQ, which reduces bias and error in simulated NH_x concentrations and deposition (Bash et al., 2010, 2013; Cooter et al., 2012; Massad et al., 2010). EPIC uses WRF meteorological data (temperature, PRECIP, relative humidity, solar radiation, and wind speed), background atmospheric CO_2 mixing ratios (consistent with WRF and CMAQ), and representative DD and WD rates derived from previous ("a priori") CMAQ simulations (not shown) to create inputs used in the CMAQ BIDI-NH_3 model. The a priori deposition rates are from a 2004 simulation year with 2011NEI emissions for the HIST period and from an average of 2048–2050 simulation years using 2040ref emissions for the FUT period. This represents an approximation of the feedback loop between EPIC fertilizer application and CMAQ BIDI-NH_3 exchange; however, this approximation has a relatively small impact compared to the WRF meteorological drivers on future EPIC agroecosystem changes. In fact, the a priori total N deposition to the CBW is only about 3% lower (not shown) compared to the annual average projected by CMAQ in the FUT period with 2040ref emissions (see Changes in Nitrogen Deposition to the Chesapeake Bay Watershed).

The FUT EPIC simulations do not assume any land use change or yield/productivity trends, and a Hargreaves estimate was used for evapotranspiration (ET) (Hargreaves & Allen, 2003), which cannot fully

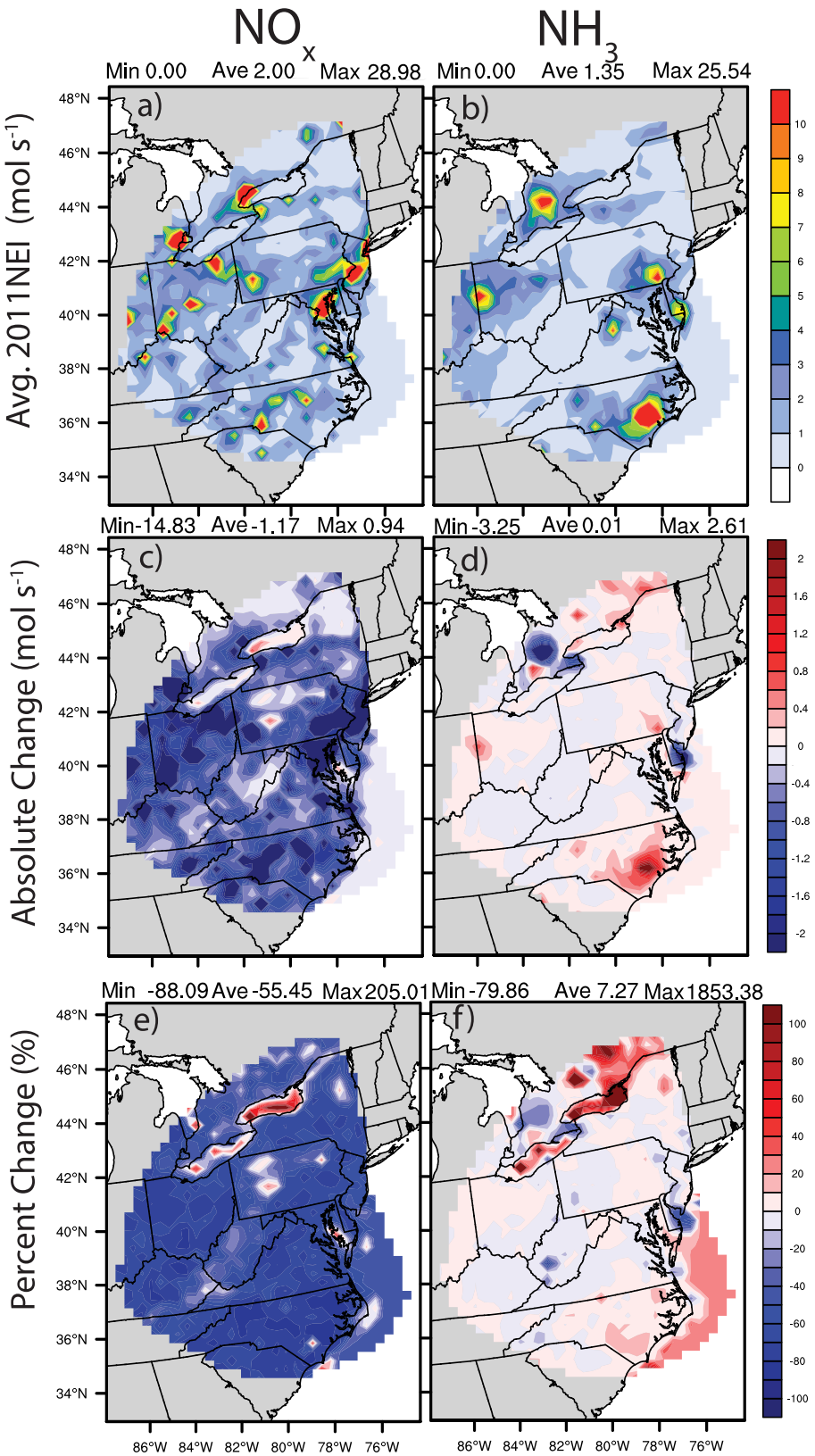

Figure 1. Spatial plots of average (a–b) 2011NEI NO_x and NH_3 emissions and their (c–d) absolute (2040ref – 2011NEI) and (e–f) relative changes (defined in Table 1) in the future for the CBA. Figures S2 and S3 also show the NO_x and NH_3 emission changes, and other gas and aerosol emissions, in the entire domain and CBW for comparison.

Table 2
Summary of the three CESM downscaled WRF-CMAQ simulation sets conducted in this study

WRF-CMAQ simulation sets		Descriptions	
Run #	**Run details** ***HIST = 1995–2004*** ***FUT = 2045–2054***	**Abbreviation**	**Impacts on future nitrogen deposition in the CBW**
1	CESM: HIST climate WRF: HIST with changing GHG levels EPIC: HIST agroecosystem CMAQ: HIST emissions (2011NEI)	HIST	None
2	CESM: FUT RCP4.5 climate WRF: FUT with changing RCP4.5 GHG levels EPIC: FUT RCP4.5 agroecosystem CMAQ: HIST emissions (2011NEI)	FUT_CLIM	Future climate and agroecosystem changes
3	CESM: FUT RCP4.5 climate WRF: FUT with changing RCP4.5 GHG levels EPIC: FUT RCP4.5 agroecosystem CMAQ: FUT emissions (2040ref)	FUT_EMIS	Future climate, agroecosystem, and emission changes

account for climate change plant response with respect to ET (i.e., no stomatal response). EPIC does, however, include biomass productivity responses in this work. The stomatal ET effects could be captured in future work if a Penman-Monteith ET method (Allen, 2005) is used rather than Hargreaves method; however, this was outside the scope as additional validation/evaluation tests are needed to be sure it is properly parameterized in EPIC for the regional CONUS domain in this application. Finally, the spin-up to the FUT climate scenarios in EPIC does not currently allow for crop variety (e.g., 60-, 90-, and 120-day corn) to change, which would influence the crop rate of maturity. The downscaled WRF and EPIC simulations are described further below (see Analysis of Simulation Dynamics).

2.3. Simulation Design

Table 2 shows the WRF-CMAQ simulation design for the HIST and FUT time periods. Three simulations include one HIST run and two FUT runs to examine the potential impacts of climate and agroecosystem (i.e., EPIC-driven) changes (FUT_CLIM) and the combined climate + agroecosystem + emission changes (FUT_EMIS) over the CBW.

3. Evaluation of Downscaled Simulations

Dynamically downscaled climate-air quality simulations using a similar methodology were typically within defined modeling performance benchmarks and consistent with results from other studies using finer-scale meteorology (Seltzer et al., 2016 and references within). Therefore, the WRF-CMAQ regional climate-air quality modeling methodology utilized here should not introduce significant bias in projected N deposition over the CBW.

The analysis and evaluation of the downscaled WRF-CMAQ focus on two regions: (1) a CBW Critical Conservation Area based on shapefiles available from the United States Department of Agriculture National Resources Conservation Service (www.nrcs.usda.gov), shaded in purple in Figure S4 (right panel) (hereafter referred to as CBW), and (2) the N airshed around and within the CBW (hereafter referred to as CBA) based on Dennis (1997) and Paerl et al. (2002), and shaded in dark green in Figure S4 (right panel). Following Paerl et al. (2002), the CBA is defined as the region within which most of the N deposition to the CBW can be attributed to changes in sources (i.e., emissions) or influences (i.e., climate) occurring within the region. The concept of a normalized range of influence of an airshed source region for watersheds is defined in Dennis (1997).

The 10-year monthly average and seasonal cumulative distribution functions of the HIST and FUT_CLIM simulations in the CBA are compared against hourly 0.31° fields from the Climate Forecast System Reanalysis (CFSR) (Saha et al., 2010) for T2 and against three-hourly 32-km North American Regional Reanalysis (NARR) (Mesinger et al., 2006) fields for precipitation (Figure S4). Figure S5 provides analogous plots for the CBW region to assess its evaluation and potential differences at the watershed scale, while

qualitative seasonal average spatial comparisons of HIST to CFSR and NARR over the WRF model domain are provided in Figures S6 and S7. The HIST T2 agrees well with CFSR and has a correlation coefficient (R) of 0.997 in both the CBA and CBW (Figures S4–S5); however, there is a systematic positive (i.e., warm) mean bias of about +1.3 K and +1.5 K in the CBA (Figure S4a) and CBW (Figure S5a), respectively. These results agree well with Figure 1 in Seltzer et al. (2016), where they used a reanalysis dataset as input to test a similar WRF downscaling methodology and found R values of 0.997–0.999 for T2 across different regions of the CONUS. The seasonal average spatial analyses of T2 from HIST also qualitatively agree well with CFSR across the WRF domain (Figure S6), and, thus, the results lend confidence to downscaling CESM RCP4.5 with WRF. Although HIST and NARR PRECIP agree well during the fall, winter, and early spring, the correlation is relatively lower at 0.595 (0.222) in the CBA (CBW) (Figures S4f and S5f), and there is a notable overprediction during the summer convective season in the eastern United States (Figure S7). See Text S3 for more statistics and detailed discussion regarding the T2 and PRECIP evaluation and potential reasons for model over- or underpredictions.

The downscaled HIST simulation has a good agreement with the weekly National Atmospheric Deposition Program (NADP) PRECIP observations with an R, root mean square error, and normalized mean bias of about 0.6, 30 mm, and +1.7%, respectively (Figure S8a; red). The HIST WD of fine particulate matter (aerodynamic diameter <2.5 μm; $PM_{2.5}$) sulfate ($WD\_SO_4^{2-}$) and nitrate ($WD\_NO_3^-$) simulations (Figures S8b–S8c) are also in good agreement with NADP, both with an R of about 0.4 and root mean square error (normalized mean bias) of about 0.4 kg/ha (−4%) and 0.3 kg/ha (−14%), respectively. Underpredictions in $WD\_SO_4^{2-}$ and $WD\_NO_3^-$ are comparable to those shown in Appel et al. (2011) in the eastern United States for the summer season. While errors in precipitation in part impact the $WD\_SO_4^{2-}$ and $WD\_NO_3^-$ bias in the eastern United States (Foley et al., 2016), there may also be impacts on the larger underpredictions in $WD\_NO_3^-$ from missing emission sources, such as missing lightning NO_x emissions. Contrary to $WD\_SO_4^{2-}$ and $WD\_NO_3^-$, the simulations of $WD\_NH_4^+$ are overpredicted compared to NADP (Figure S8d). Bash et al. (2013) show that including the EPIC and BIDI-NH_3 model coupling in the CMAQ model leads to increases in WD_NH_x (WD_NH_3 + $WD\_NH_4^+$) in the eastern United States, which likely contributes to this overprediction in $WD\_NH_4^+$. See Text S4 for more detailed information regarding these evaluations and discussion of the pertinent reasons behind model over and underpredictions.

4. Results of the Model Projections

The following subsections include analysis and discussion of the climate and agroecosystem changes that are important in both the CBA and CBW regions and the ultimate impacts on N deposition to the CBW for the FUT_CLIM and FUT_EMIS scenarios.

4.1. Changes in Downscaled Climate

Figure 2 shows WRF HIST and FUT_CLIM predictions of 10-year and annual averaged T2, 2-m water vapor mixing ratio (Q2), 10-m wind speed (WSPD10), planetary boundary layer height (PBLH), instantaneous downward shortwave radiation taken at the surface (SWDNB), and 10-year and annual total PRECIP over the CBA (CBW region Figure S10). Figure 3 further shows the 10-year average spatial plots of HIST values and absolute (FUT_CLIM − HIST) and relative change ([(FUT_CLIM − HIST) /HIST] × 100%) plots for the CBA region (CBW region Figure S11). For additional analysis of the meteorological variables' seasonal changes, Figures S12–S17 show monthly spatial difference (absolute and relative) plots for both the CBA and CBW regions.

The 10-year average FUT_CLIM T2 and Q2 reflect pronounced and widespread increases in the CBA and CBW, which show CBA area-averaged absolute (relative) increases of 1.6 K (14% in °C) and 0.8 g/kg (9%), respectively (Figures 2a–2d and 3a–3f). The CBW area-averaged increases are comparable to those in CBA, at 1.7 K (14% in °C) and 0.8 g/kg (10%), respectively (Figure S11). In fact, the widespread increases in T2 and Q2 in the CBA and CBW occur during most seasons of the year, except for a few months in late fall and winter (November, January, and February) (Figures S12 and S13). Consistent with Figure S4a, the strongest warming on average occurs in the spring, with a maximum T2 increase in March (3.1 K for CBA and 3.3 K for CBW; Figures S12a–S12b), while the most significant moistening of the atmosphere occurs in the summer and fall, with maximum Q2 increases in July–September (both CBA and CBW about 1.2–1.3 g/kg; Figures S13a–S13b). Similar warming and moistening patterns have been shown in other applications of

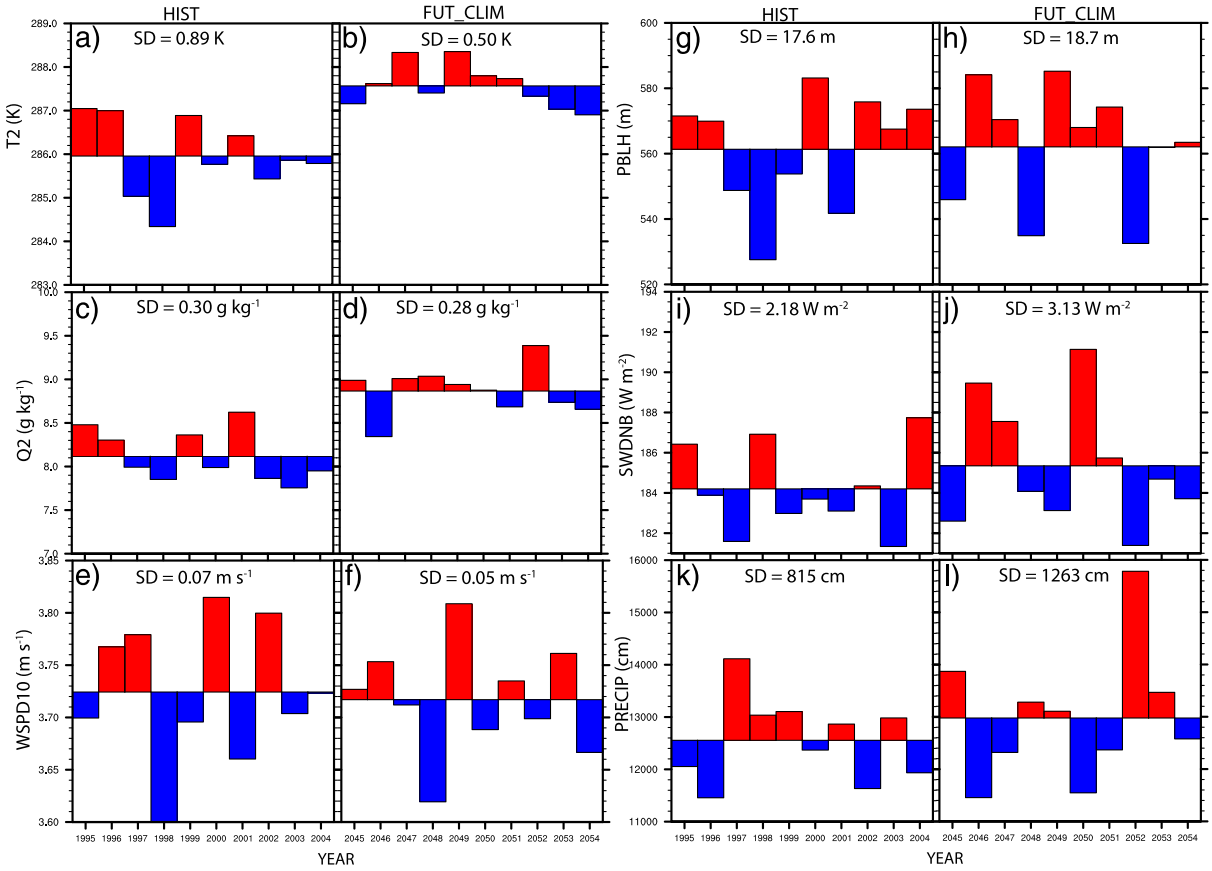

Figure 2. Comparisons of downscaled WRF HIST and FUT_CLIM predictions for 10-year (horizontal lines) and annual averages of (a–b) T2,(c–d) Q2, (e–f) WSPD10, (g–h) PBLH, (i–j) SWDNB, and (k–l) PRECIP area-averaged over the CBA. Annual average values above and below the 10-year average are shown in red and blue, respectively. The CBA region analyzed is shown in the green-shaded area in the shapefile panel in Figure 3 and more precisely shown in the model spatial analysis in Figure S4. The standard deviations used to address the interannual variability are also shown.

downscaled global RCP4.5 scenarios to regional WRF simulations over North America, with approximate domain-wide average increases of about 1 K and 0.2 g/kg based on estimates taken from a number of different studies that compared future climate changes out to about 2050 (Nolte et al., 2018; Trail et al., 2013; Yahya et al., 2017), with additional warming over CONUS (increase >1–2 K) projected under RCP4.5 late in the 21st century (Nazarenko et al., 2015; Nolte et al., 2018; Separovic et al., 2013). In a more direct comparison, Figure 1 of Yahya et al. (2017) shows widespread increases in a similar future period (2046–2055) for T2 and Q2 across CONUS, with substantial spatial variability (grid resolution of 36 km), and an approximate increase of about 1.5–2.0 K and 0.8–1.0 g/kg near the CBA and CBW regions. The results in our work are comparable to Yahya et al. While there is large interannual variability about the 10-year average for T2 and Q2 (Figure 2), the variability is less extreme in the FUT_CLIM compared to HIST for T2, as the respective standard deviation is reduced by almost half in the FUT_CLIM in the CBA (Figures 2a–2b) and CBW (Figures S10a–S10b). The interannual variability is nearly constant/slightly lower for Q2 from the HIST to the FUT_CLIM (Figures 2c–2d and S10c–S10d). The interannual variability is in part driven by using yearly changing RCP4.5 GHG mixing ratios in the downscaled WRF simulations for both HIST and FUT_CLIM (see section 2.2), which has not been applied in some previously discussed studies due to the relatively recent implementation of dynamic CAM GHGs for use in WRF (since Version 3.5). Considering that NH_3 air-surface fluxes in the CMAQ BIDI-NH_3 model are a strong function of atmospheric (canopy) temperature (Bash et al., 2013), the FUT_CLIM increases in T2 suggest a direct climate impact on future N deposition changes to the CBW. Changes in T2 also impact the thermodynamic formation of $PM_{2.5}$ ammonium nitrate (NH_4NO_3), especially in the winter, which can alter the future interplay between the atmospheric total (wet + dry) deposition of oxidized ($O_xN \sim NO_x + NO_3^-$) and reduced ($NH_x \sim NH_3 + NH_4^+$) N species.

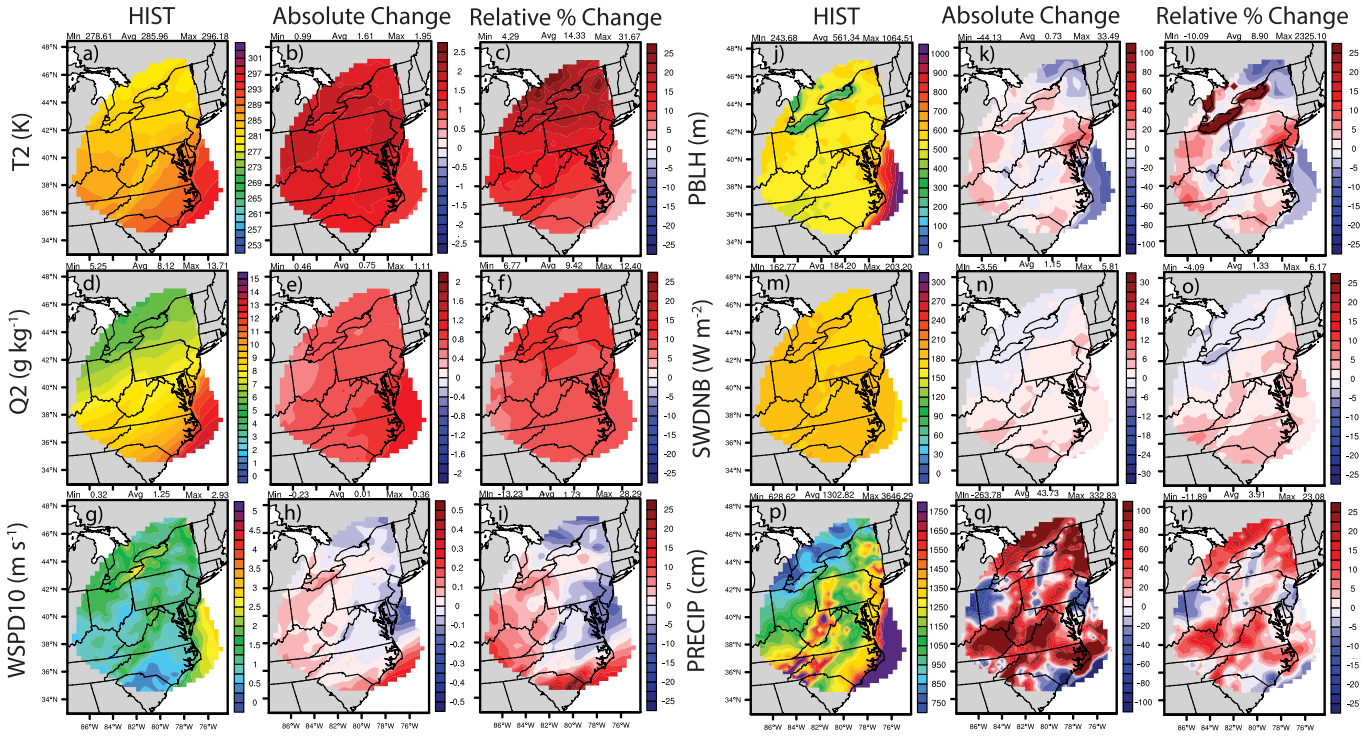

Figure 3. Comparisons of downscaled annual average WRF HIST and absolute and relative changes (FUT_CLIM – HIST) for (a–c) T2, (d–f) Q2, (g–i) WSPD10, (j–l) PBLH, (m–o) SWDNB, and total (p–r) PRECIP over the CBA. The average, maximum, and minimum values over the CBA region are shown above each panel. The relative (%) changes for T2 in (c) are performed based on Celsius temperatures (°C = °K – 273.15).

Changes in mean daily T2 used in EPIC will change the vegetation and the timing of crop development (growing season), which can change temporal patterns of nutrient use/demand and soil erosion and nutrient loss. Increased/decreased temperature stress will also impact vegetation growth and development (magnitude as well as timing), which will, in turn, impact fertilizer demand and timing (see section 4.2 for more details).

There is relatively more interannual and interseasonal variability for the other meteorological variables compared to T2 and Q2, in conjunction with slight 10-year average FUT_CLIM decreases for WSPD10, and increases in PBLH, SWDNB, and PRECIP in the CBA and CBW (Figures 2e–2l, 3g–3r, S10, and S14–S17). The interannual variability (i.e., standard deviation) slightly decreases for WSPD10, stays nearly constant/slightly increases for PBLH and SWDNB, and moderately increases for PRECIP from the HIST to the FUT_CLIM in the CBA. While there are widespread increases in WSPD10 in the western and northern United States that generally trend with the largest increases in T2 under RCP4.5 (not shown), there are both WSPD10 increases and decreases in the CBA (area-average approximately +0.01 m/s; +1.7%) and predominantly decreases in the CBW (area-average approximately −0.04 m/s; −3.1%). The WSPD10 changes are also in agreement with Yahya et al. (2017) for these regions. Changes in WSPD10 in the CBA and CBW are important because (1) they directly impact wind erosion and sediment/N loss in EPIC that can result in NH_3 fertilizer application changes coupled to CMAQ-BIDI-NH_3 exchange, and future N deposition efficiency changes to the CBW and (2) they have additional implications for understanding how changes in future WSPD10 forcing in the CBW may affect changes in wind stress dynamics, as well as other nutrient loading and cycling in the Chesapeake Bay (Fisher et al., 2015). In fact, some of the largest WSPD10 decreases occur in the estuary region of the CBW (Figure S11i), but there is significant interseasonal and spatial variability in the direction of WSPD10 change (Figure S14b).

The changes in PBLH are strongly tied to changes in T2 in the CBA and CBW, as the warmer future climate dominates the 10-year average PBLH increase, despite a slight decrease in the average WSPD10 (more prolifically in the CBW). Furthermore, in the FUT_CLIM, all years above (below) the average for T2 are also associated with an above (below) average PBLH, except in 2054. The small annual average PBLH increase in the FUT_CLIM of 1–6 m in the CBA and CBW also approximately agrees with Yahya et al. (2017) for a

similar region, where they show a <10-m increase. An increase in PBLH will help to enhance the dispersion of N containing pollutants, thus helping reduce their concentrations and potential deposition in the future; however, we note that there is also significant interseasonal variability in the PBLH changes, where there are numerous months (e.g., March–July and November) that show an area-average decrease in PBLH for the FUT_CLIM (Figure S15a–S15b).

The overall annual average increases in SWDNB are slight, with an absolute (relative) increase in the CBA of 1.2 W/m^2 (1.6%) and CBW of 1.6 W/m^2 (1.8%), and are similar but on the low-end of the increases shown in Trail et al. (2013) of 0–6 W/m^2 over North America. The changes in SWDNB are inherently tied to changes in cloud variables, both of which (not shown for clouds) have significant spatiotemporal variability (Figures S16a–S16b). There appears to be a trend, however, of predominant large increases in SWDNB in the late spring-summer (May–August) and moderate decreases in the winter and early spring (December–April). The warmer (T2) and moister (Q2) late spring-summer months in the FUT_CLIM may result in more subgrid convective clouds, less overall cloud fraction, and more shortwave radiation reaching the surface, while the opposite is true in winter (except in January) when the moister atmosphere leads to generally more grid-scale cloudiness and less SWDNB. Such changes in total cloud fractions in the model, however, are inherently skewed by artifacts of the subgrid cloud parameterization. Nonetheless, changes in SWDNB can impact future N deposition to the CBW in two main ways: (1) changes in SWDNB can influence the photochemical impacts on important atmospheric species, either directly or indirectly impacting some N species (e.g., easily degradable NO_2), and (2) changes in the amount of deep/moist convective clouds result in changes to the frequency and intensity of RC and associated NO_x emissions through the CMAQ lightning NO_x parameterization.

EPIC vegetative growth is also a function of photosynthetic active radiation, and changes in SWDNB can change vegetation growth and development and subsequent fertilizer demand and timing.

The 10-year average of total annual PRECIP tends to increase slightly for FUT_CLIM compared to HIST and has significant interannual (Figures 2k–2l) and spatiotemporal variability (Figures 3p–3r and S17a–S17b) over the CBW. Overall there is an annual absolute (relative) increase in PRECIP of about 44 cm (3.8–3.9%) in the CBA and CBW, where other previous studies show qualitatively similar PRECIP increases over the eastern United States for the RCP4.5 and other scenarios (e.g., Separovic et al., 2013; Trail et al., 2013; Wang & Kotamarthi, 2015; Yahya et al., 2017). The interseasonal variability in PRECIP (Figures S17a–S17b) is in loose agreement with the direction in SWDNB changes due to cloud variable impacts, where average monthly increases (decreases) in PRECIP are associated with decreases (increases) in SWDNB; however, there is significantly more spatial variability in PRECIP than SWDNB. The changes in PRECIP have a direct impact on the WD of N species to the CBW, and this relationship will be explored more in later sections.

EPIC vegetation growth is also a function of moisture stress; if there is too little PRECIP, growth is reduced (as well as N demand). If there is too much PRECIP and soils become saturated, this causes aeration stress (i.e., plants are drowning) that will reduce vegetation growth and N demand. The bottom line is that if temperature, photosynthetic active radiation, and precipitation variability increase, stress variability will increase, and then so might N demand and applications (i.e., become more variable in both timing and magnitude).

4.2. Changes in Agroecosystem Processes

There are over 87,000 working farms in the CBW, which include farming practices such as dairy and beef cattle, poultry operations, grain and produce production, and tree and shrub nurseries (www.chesapeakebay.net). Thus, the farming practices and fertilization characteristics modeled by EPIC, and coupled to CMAQ BIDI-NH_3 exchange, are important to the simulations of future changes in total N deposition in the CBW. Crop-specific EPIC simulated inorganic NH_3 fertilization rates, timing, depths (dictated by N form/application method), and managed soil pH values are used as inputs to the CMAQ BIDI-NH_3 model (Cooter et al., 2012). More specifically, EPIC estimates of the NH_3 application rate (L1_ANH3 and L2_ANH3) and layer Łcontent (L1_NH3 and L2_NH3) in applied fertilizers at two depths of 1 and 5 cm are input to the CMAQ BIDI-NH_3 model's calculation of the soil NH_4^+ pool, H^+ changes, and soil emission potential (Γg, defined as $[NH_4^+]/[H^+]$) for different agricultural LU categories (Bash et al., 2013; Cooter et al., 2012).

Future changes to CO_2 (higher in FUT_CLIM), atmospheric deposition, and the downscaled WRF simulation output can impact EPIC predictions of NH_3 fertilizer application rates (L1_ANH3 and L2_ANH3) and layer

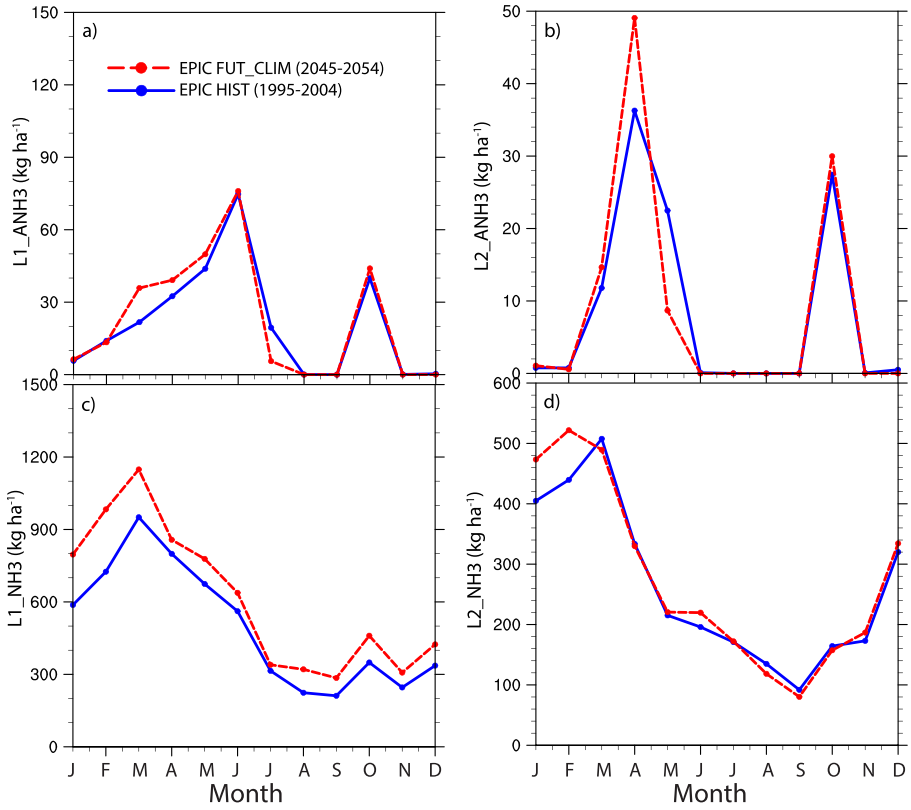

Figure 4. Ten-year average monthly values of HIST (blue) and FUT_CLIM (red) CBA area-totaled NH_3 (a–b) fertilizer application rate (L1_ANH3 and L2_ANH3) and (c–d) layer content (L1_NH3 and L2_NH3) for the sum (rainfed + irrigated) of all 2006 NLCD-BELD4 crop types.

content (L1_NH3 and L2_NH3), which can directly alter the dynamics of CMAQ BIDI-NH_3 exchange (i.e., NH_3 deposition vs. evasion) in the CBA, and lead to changes in the resulting N deposition in the CBW. We note that both future EPIC simulations (Table 2: FUT_CLIM and FUT_EMIS) use the average 2048–2050 CMAQ deposition that is reflective of the 2040ref emissions changes and that this approximation also has a relatively small impact compared to the WRF meteorological drivers on future EPIC agroecosystem changes. Figure 4 shows the 10-year average HIST and FUT_CLIM monthly values of total L1_ANH3, L2_ANH3, L1_NH3, and L2_NH3 summed across all crop types in the CBA. Figure S18 shows the same analysis for the CBW, while Figures S19–S20 show similar fertilizer application and content plots for the total (rainfed + irrigated) hay, alfalfa, other_crop/mixed grains (including spring rye, flaxseed, forage seed, mustard seed, sunflowers, canary seed, ginseng, buckwheat, sugar beets, caraway seed, triticale, and other field crops), corn, soybeans, and wheat (includes both spring and winter wheat types) crop categories (and their respective fractions compared to the sum of all crops), as these crop categories cover the largest fractional areas in the CBA and CBW (see spatial plots based on the 2006 NLCD (National Land Cover Database; Data found at https://www.mrlc.gov/)-BELD4 (Biogenic Emissions Landuse Database Data found at https://www.cmascenter.org) in Figures S19–S20), while the sum of all other crop types represent <0.5% of the average LU cover.

As the timing of fertilizer applications is tied to temperature, warmer spring T2 in the FUT_CLIM compared to HIST (Figures S4a and S12) results in earlier (March–April) planting in the CBA, with most fertilizer applications happening at the topsoil layer of L1_ANH3, but also slightly earlier applications in L2_ANH3, which is typically a pelletized or some combined dry fertilizer product (Figures a–b and S18a–S18b). The timing of higher L1_ANH3 earlier in spring is due to a combination of hay (40%), corn (40%), and soybean (20%) crops in the CBA and CBW (Figures S19a–S19b). The earlier planting dates are elucidated in Figures S21a–S21b, where there are widespread decreases (FUT_CLIM – HIST) in the 10-year average of yearly total planting Julian dates (IPLD) summed across all crop types. The faster summer drop in L1_ANH3 by July is driven

by earlier or more quickly maturing crops and an earlier harvest of corn (80%) and other_crop/mixed grains (20%), which is also shown in Figures S21a–S21b with similar plots of earlier (i.e., negative FUT_CLIM – HIST) total harvest Julian dates (IHVD). The faster late spring drop in L2_ANH3 by May is similarly due to earlier harvest of corn (60%) and other_crop/mixed grains (40%) in the CBA and CBW (Figures S19a–S19b). We note that a reason why the other_crop/mixed grains may account for such a large fraction of the total is because it is modeled as corn, which may or may not be correct for certain grains, and is certainly an approximation for small grains.

The slightly larger peak in L1_ANH3 in June is solely due to corn crops, while the considerably larger peak in L2_ANH3 (injected anhydrous NH_3 fertilizer mainly associated with corn production) for FUT_CLIM by April is due to a combination of corn (80%) and other_crop/mixed grains (20%) (Figures S19a–S19b). An initial hypothesis is that the increase in both L1_ANH3 and L2_ANH3 peaks is driven by higher productivity in spring (due to higher CO_2) and thus higher N demand. Figures S21a–S21b show, however, that there are widespread decreases in forage yields (YLDF) and grain yields (YLDG) for corn, as well as widespread decreases in YLDG for other_crop/mixed grains for the FUT_CLIM compared to HIST (YLDF = 0 for this crop category). The decrease in yields is largely due to an increase in number of water stress days (Figures S21a–S21b). Thus, it is possible that the larger peaks in L1_ANH3 and L2_ANH3 are due to increased PRECIP in the FUT_CLIM (Figures 2, 3, S11, and S17a–S17b), greater N losses from runoff due to approximately greater PRECIP intensity in EPIC, and thus additional N demand. This is confirmed by the widespread increases in the projected N loss due to runoff (QNO3) in both CBA and CBW (Figures S21a–S21b). As N deposition goes directly in the layer 2 soil pools, there may be additional impacts on the enhanced L2_ANH3 peaks (maximized in April) due to reduction in anthropogenic NO_x emissions (see Emission Projections to 2040) that lead to decreases in future total N deposition (primarily from O_xN reductions). Finally, the fall and winter fertilizer applications are essentially unchanged between HIST and FUT_CLIM, but there is a slightly larger peak for L1_ANH3 and L2_ANH3 in October that is dominated by the wheat and corn crops in CBA and CBW (Figures S19a–S19b).

There are consistently larger L1_NH3 in the FUT_CLIM compared to HIST (except for July) (Figures 4c and S18c), which is driven by a combination of hay (January–March and July–August; average ~30%), corn (January–June and September–December; average ~25%), wheat (January–March and October; average ~20%), alfalfa (January–September; average ~15%), and other_crop/mixed grains (January–June; average ~10%) (Figures S20a–S20b). There is considerably less of a difference for L2_NH3, with the largest FUT_CLIM increase in the winter months of January–February (Figures 4d and S18d) due mainly to hay, corn, and wheat (total average ~70%) and a smaller contribution from alfalfa, other_crop/mixed grains, and soybeans (total average ~30%) (Figures S20a–S20b). Since there is little to no difference in the preceding fall L2_ANH3 application to the L2_NH3 increases in the winter, an initial hypothesis for the larger FUT_CLIM values in layer 2 is that potentially less soil moisture in the FUT_CLIM leads to less N percolation (PRKN) or denitrification (DN). Figure S21 shows widespread FUT_CLIM increases in PRKN and DN, however, which is likely due to increased average PRECIP in the FUT_CLIM. A more likely possibility for the larger L2_NH3 in winter is more rapid N mineralization because of more plant residue, which is an EPIC biomass response to the increased CO_2 for the FUT_CLIM runs. Figures S21a–S21b confirm the widespread increases in the future N (GMN) and humus mineralization (NMN) (enhances soil inorganic N), compared to much smaller (~factor of 5) increases in the DN (reduces soil inorganic N) for the sum of all crops in the CBA and CBW. These factors are consistent with the increased T2 and adequate Q2 in the FUT_CLIM (Figures 2, 3), which in essence "speed-up" biogeochemical cycling in the future EPIC simulations.

The enhanced surface pattern of L1_NH3 for FUT_CLIM does not correlate particularly well with application of L1_ANH3; and thus, it is not a direct result of increased fertilizer application to the surface in the FUT_CLIM. The increase in L1_NH3 for the FUT_CLIM is due to a combination of impacts from (1) enhanced GMN and NMN across all months; (2) increased total soil organic carbon, which is a metric for enhanced N residue and mineralization; and (3) increased N fixation (possibly as a response to decreased N deposition) from prolific N fixation crops such as alfalfa occurring across many months (Figures S21a–S21b). The increases in NH_3 fertilizer application and soil content shown in Figure 4 have impacts on BIDI-NH_3 exchange and N deposition in the CBW (see Changes in Nitrogen Deposition to the Chesapeake Bay Watershed).

4.3. Changes in Nitrogen Deposition

Projected changes in the climate/agroecosystem under the RCP4.5 scenario (sections 4.1 and 4.2) and projected changes in regional 2040ref emissions inputs (section 2.2.3) impact the future projections of N deposition to the CBW. There is also significant spatial variability in future NO_x and NH_3 emissions, as well as spatial and seasonal variability in the future climate/agroecosystem changes. In this section we analyze the absolute and relative (%) changes (Figure S22) in total deposition (TD) of O_xN (TD_O_xN), NH_x (TD_NH_x), and total N (TD_N = TD_O_xN + TD_NH_x) to the CBW driven by the climate and agroecosystem changes (FUT_CLIM) and the combined FUT_CLIM and emissions (FUT_EMIS) changes for all four seasons (Figure 5).

When accounting for FUT_CLIM changes only, there are average increases in the TD_N during all seasons in the CBW (Figures 5a2–5d2), which during the winter and spring are primarily driven by a combination of TD_O_xN and TD_NH_x increases (Figures 5e2–5f2 and i2–j2), and during the summer and fall are primarily due to increases in TD_NH_x (Figures 5k2–5l2). There are relatively small decreases in TD_O_xN in the summer and fall for FUT_CLIM (Figures 5g2–5h2) and an area of larger TD_NH_x decreases, which contribute to areas of decreased TD_N in the summer and fall. This pattern of widespread increases in TD_N for FUT_CLIM is strongly driven by widespread regions of increased PRECIP and wet deposition to the CBW (Figures 3q–3r and S11q–S11r), and likewise there is a spatially similar area of PRECIP and TD_N decreases during the summer in the CBW (Figure S17b). The larger relative increases in TD_NH_x compared to TD_O_xN (some average decreases) during all seasons in FUT_CLIM are in part due to widespread increases in T2 in the CBA and CBW (Figures 3b–3c and S11b–S11c), which drive a thermodynamic partitioning (i.e., volatilization effect) toward enhanced NH_3 concentrations in the atmosphere, and consequently more DD of NH_3 compared to the O_xN gases.

The higher EPIC L1_ANH3 and L1_NH3 (topmost soil layer fertilizer application rate/content) in the FUT_CLIM scenario (Figures 4a and 4c) are also indicative of a higher initial soil NH_4^+ pool and soil emission potential, Γ_g (modeled in CMAQ as a function of fertilizer application following Massad et al., 2010) and consequently a higher soil compensation point (C_g). The higher C_g contributes to a higher overall canopy NH_3 compensation point (C_c) in CMAQ's BIDI-NH_3 exchange model (Bash et al., 2013), which may lead to enhanced NH_3 evasion in areas just outside of the CBW, especially those regions with high NH_3 emissions estimates from fertilizer application due to agricultural management practices (e.g., elevated hay and corn crop percentages in CBA; Figure S20a). This could theoretically lead to more TD_NH_x in the CBW downstream of such areas in the CBA.

Including the effect of the projected 2040ref emissions in the FUT_EMIS simulations results in a widespread decrease in TD_N in the CBW, with an area-averaged seasonal range in absolute (relative %) decreases of 0.52–0.62 kg/ha (17–28%) (Figures 5a3–5d3). This is in stark contrast to the FUT_CLIM simulations and clearly demonstrates the benefits of decreased anthropogenic NO_x emissions in the 2040ref case. Decreases in TD_N in FUT_EMIS case are largely dominated by decreases in TD_O_xN, which have a seasonal range of about 0.54–0.60 kg/ha (42–48%) in the CBW (Figures 5e3–5h3). Despite the widespread decreases in TD_N and TD_O_xN, there are widespread increases in TD_NH_x (except in the summer from enhanced PRECIP and WD) due to relatively constant (or slightly increasing) agricultural NH_3 emissions in the projected 2040ref case (compared to decreases in NO_x and SO_x emissions), which lead to a seasonal range of about −0.02 to +0.14 kg/ha (−0.5 to +16%) in the CBW. While there are definitive climate and agroecosystem impacts on future TD_N changes (mainly increases), the TD_N changes (mainly decreases) in FUT_EMIS in the CBW are dominated by future decreases in NO_x emissions and TD_O_xN, in conjunction with a shifting paradigm of increased NH_3 emissions and TD_NH_x.

This shift toward relative decreases in oxidized N deposition and increases in reduced N deposition has an impact on the seasonal TD_N deposition budget, which includes relative (%) changes to the WD and DD of O_xN and NH_x in the CBW (Figure 6). The associated absolute changes are shown in Figure S23.

There are minimal changes in the relative contributions to the TD_N budget in the FUT_CLIM scenario (under constant emissions) compared to HIST, with only slight (~1–3%) decreases in DD_O_xN and DD_NH_x (winter only) and increases in WD_NH_x and WD_O_xN (winter only) proportions in the CBW. There are larger changes in the TD_N budget in the FUT_EMIS scenario, with decreases in the proportion

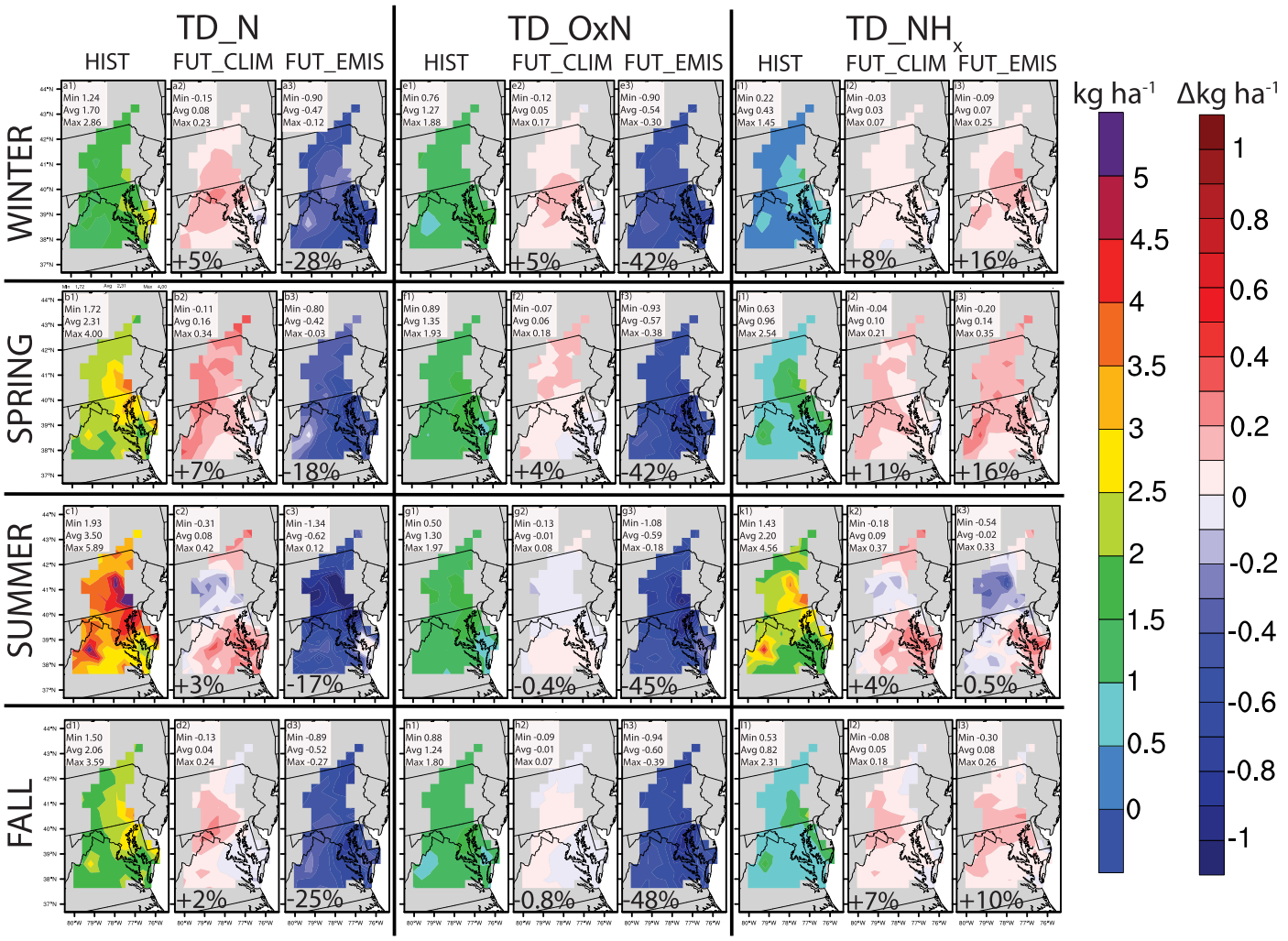

Figure 5. Spatial plots of the 10-year average seasonal totals (HIST; column 1) and absolute differences (FUT_CLIM, column 2, and FUT_EMIS, column 3) for (a–d) TD_N, (e–h) TD_O_xN, and (i–l) TD_NH_x in the CBW. The average relative changes (defined in Table 1) are shown in the bottom left-hand corner of each FUT_CLIM and FUT_EMIS panel (based on Figure S22).

of DD_O_xN (~10–15%) and WD_O_xN (~2–3%) and increases in DD_NH_x (~10–13%) and WD_NH_x (~2–6%). The most notable is the shift to an increase in the DD_NH_x proportion (annual CBW average ~12%), where the increases in DD_NH_x are dominated by increases in DD_NH_3 (DD_NH_3 is much faster than DD_NH_4^+), which are larger than the increases in average NH_3 emissions in the CBA (~7%; Figure 1f) and decreases in the CBW (~1%; Figure S3f), due to a reduction of ambient NH_4^+ aerosols from SO_x and NO_x 2040ref emission controls (i.e., more NH_3 available to deposit).

5. Summary and Discussion

Decreases in atmospheric emissions of NO_x and the subsequent change in deposition have been documented as one of the largest causes of reductions of nitrogen (N) loading to the CBW (Shenk & Linker, 2013). Here we estimate that atmospheric N deposition is projected to continue to decrease from the HIST (1995–2004) period (representative of the 2011 emission year) levels due to emission reductions by approximately 21% despite a small, approximately 4%, atmospheric penalty associated with changes in climate by the FUT (2045–2054) period (midpoint year of 2050, representative of 2040ref emission projections) levels (Table 3).

The deposition changes for individual N containing pollutants, however, are not proportional. We estimate that the total N deposition will follow the historical trend (Li, Schichtel, et al., 2016) of increases in the

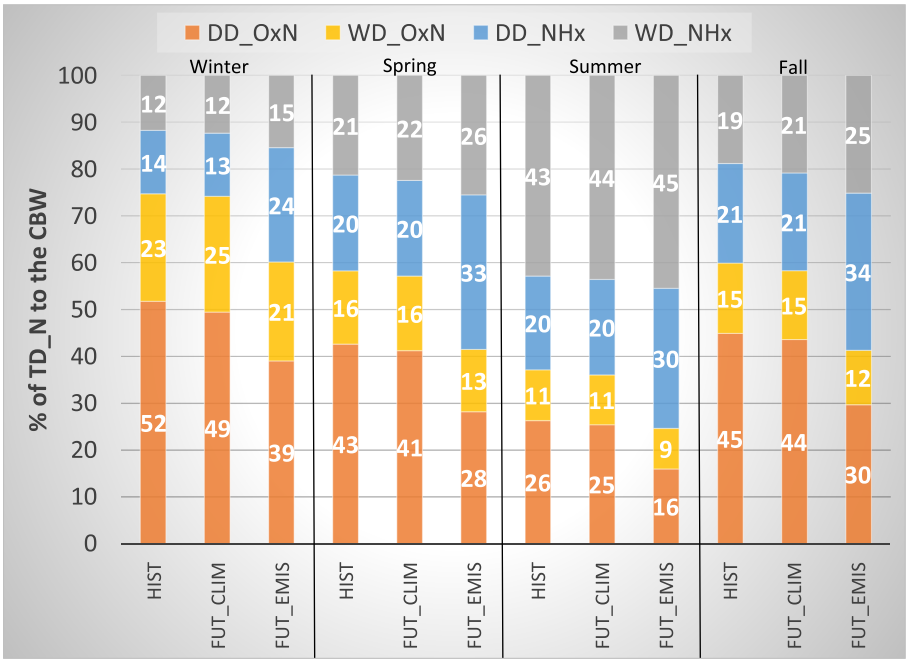

Figure 6. Stacked bar plots of the 10-year average (HIST, FUT_CLIM, and FUT_EMIS) percent of DD_O_xN (red), WD_O_xN (yellow), DD_NH_x (blue), and WD_NH_x (gray) of the seasonal total N deposition (TD_N) to the CBW.

reduced N fraction (Figure 6). This is primarily due to the decreased NO_x emissions, while NH_3 emissions have remained relatively static (Table 1). Atmospheric aerosol processes also play a role in this change. Historical NO_x and SO_x reductions have decreased ambient concentrations of $PM_{2.5}$ by approximately 45% in the Mid-Atlantic United States since 2000 (https://www.epa.gov/air-trends/). The decrease in the atmospheric aerosol burden decreases the amount of NH_3 that can form NH_4 aerosols, which leaves more gaseous NH_3 in the atmosphere that has a much faster deposition velocity than particulate NH_4^+ and consequently increases both the ambient NH_3 and NH_3 DD near agricultural sources. This has been observed in satellite observations (Warner et al., 2017), while our projections are further confirmed by other recent historical estimates in Zhang et al. (2019) and additional "on-the-books" projections (with a static climate) to 2030 that project the NH_x portion of the total N deposition to continue to increase despite a reduction in the total N load (Figure 7).

Changes in climate are expected to contribute to reductions in dissolved oxygen and further stress coastal water quality (Breitburg et al., 2018). Projected decreases in the annual average surface wind speed, and increases in temperature and precipitation in the simulations here, suggest a potential increase in future conditions associated with hypoxia in the Chesapeake Bay. The atmospheric loading of N to the CBW, however,

Table 3
Magnitude of TD_N over the total areas of the CBW, the bay and its tributaries, and tidal wetlands for HIST, FUT_CLIM, and FUT_EMIS

CBW region	Total CBW area	Bay and tributaries	Tidal wetlands area
Area (ha)	16,575,939	1,160,057	114,931
Average annual HIST TD_N (kg/ha)	9.6		
Annual total HIST TD_N (kg)	159,129,010	11,136,544	1,103,336
Average annual FUT_CLIM TD_N (kg/ha)	10.0 (+4%)		
Annual total FUT_CLIM TD_N (kg)	164,930,589	11,542,564	1,143,562
Average annual FUT_EMIS TD_N (kg/ha)	7.6 (−21%)		
Annual total FUT_EMIS TD_N (kg)	125,479,855	8,781,629	870,026

Note. The average annual TD_N in kg/ha is based on the spatial average over CBW, and relative change (%) for the FUT_CLIM and FUT_EMIS is also shown in parenthesis.

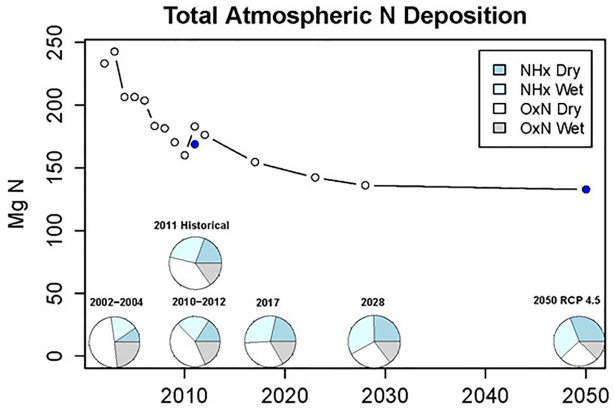

Figure 7. Total N deposition to the CBW from 2002 to 2050, the dotted line, and the proportion of deposition as NH_x dry deposition, NH_x wet deposition, O_xN dry deposition, and O_xN wet deposition, pie charts. The simulations done in this study are represented by the blue points (i.e., represented by 2011 emissions year and the midpoint of FUT period, 2050), and the other historical simulations are described in Zhang et al. (2019). Additional projections to about 2030 are based on "on-the-books" emission projections with a static climate.

are projected to decrease from current estimates (Figure 7), where current modeling estimates indicate that the nutrient loading is the main mechanism driving hypoxia in the Chesapeake Bay (Li, Lee, et al., 2016). Additionally, there is a climate penalty associated with NH_x deposition, where increases in ambient temperatures have been shown to increase the NH_3 emissions in the bidirectional NH_3 (BIDI-NH_3) modeling framework employed here and increases in temperature have been associated with higher atmospheric NH_3 concentrations (Sutton et al., 2013). This is captured in the NH_3 deposition increases from our simulations with incremental changes in climate and climate + emissions (Figure 5).

We note that there is a potential for economic uncertainty in the EPIC simulations, which has an impact on CMAQ BIDI-NH_3 exchange and projections in N loading to the CBW. In the real world, farmers are not able to predict the correct amount of fertilizer to apply to meet demand, and thus the ability to predict the amount to put on each year becomes more uncertain. This can lead to either underapplication (some potential yield loss, as more N would lead to higher yields) or overapplication in different regions, which represents increased economic costs (e.g., putting on N when crops cannot use it because of stress and greater losses to the environment because the crops are not taking up the N). Furthermore, while there is confidence in the EPIC sensitivity/response of the biogeochemical system and direction of change in the HIST and FUT scenarios, certain aspects of the EPIC processes (e.g., nitrification) are currently being improved that would affect the N budget and overall confidence in predicted magnitudes for the changes.

In conclusion, a modeling framework has been developed here that allows for an improved estimation of the impact of climate change, agricultural practices, and emission reductions on N deposition to the Chesapeake Bay. Our application of a regional-scale meteorological model forced by large-scale motions of the global CESM has yielded deposition results that are comparable to retrospective model simulations of Zhang et al. (2019) (and the "on-the-books" projections to 2030) that used meteorological data assimilation (Figure 7). We estimate that the atmospheric loading to the CBW will decrease by approximately 21% from 2011 values by about 2050. This includes approximately a 4% offset in deposition (Table 3) due to the change in climate (e.g., temperature, precipitation, and wind speed effects). The composition of the N deposition to the Chesapeake Bay is becoming increasingly dominated by NH_x due to reductions in NO_x and SO_x emissions and the reduced atmospheric aerosol burden associated with the emission reductions. The shift is likely to alter the biogeochemical cycling of the deposited N and may be more bioavailable for algae. Finally, the importance of reduced anthropogenic emissions of NO_x on future N deposition loading to the CBW cannot be overstated.

To address the uncertainties involved in model scale and land use impacts, future work includes running a similar configuration of the downscaled WRF-CMAQ model with additional nested domains at finer scales (e.g., $\leq$12 km) while also incorporating the effects of land use changes. This will allow for an assessment of the sensitivity to model grid scale and to investigate a more comprehensive interplay between climate, emissions, *and* land use changes on N deposition to the CBW. The effects of model scale and land use change on the results, however, will likely be a smaller driver than the strong anthropogenic emission signal shown in this work.

Disclaimers

Although this work has been reviewed and approved for publication by the U.S. EPA, it does not necessarily reflect the views and policies of the agency.

The scientific results and conclusions, as well as any views or opinions expressed herein, are those of the author(s) and do not necessarily reflect the views of NOAA or the Department of Commerce.

Acknowledgments

This research was performed while Patrick Campbell held a National Research Council Research Associateship Award at the U.S. Environmental Protection Agency. We thank Christian Hogrefe and Robert Pinder (U.S. EPA) for providing valuable comments on a draft of this manuscript. We further acknowledge use of the CFSR and NARR reanalysis fields and the NADP network for their data records. The raw and processed CESM and WRF-CMAQ simulation data are very large (total size >5 TB) and are freely available in two different ways: (1) On the local U.S. EPA repositories that can be directly transferred via SFTP or SCP in pieces or manually copied in their entirety and provided via external hard drives and (2) on a publicly available repository/transfer in pieces or via another high-speed file transfer service such as Globus (https://www.globus.org/data-transfer). The regional WRF-CMAQ model code used in the presented analyses is available at https://zenodo.org/record/1472755 (DOI: 10.5281/zenodo.1472755). The CESM code is available for download on the Earth System Community Modeling Portal's GitHub (https://github.com/ESCOMP/cesm).

References

Allen, R. (2005). Penman-Monteith Equation. In Daniel Hillel (Ed.), *Encyclopedia of soils in the environment* (pp. 180–188). Columbia University, New York, NY, USA: Academic Press. https://doi.org/10.1016/B0-12-348530-4/00399-4

Appel, K. W., Foley, K. M., Bash, J. O., Pinder, R. W., Dennis, R. L., Allen, D. J., & Pickering, K. (2011). A multi-resolution assessment of the Community Multiscale Air Quality (CMAQ) model v4.7 wet deposition estimates for 2002–2006. *Geoscientific Model Development*, *4*, 357–371. https://doi.org/10.5194/gmd-4-357-2011

Appel, K. W., Pouliot, G. A., Simon, H., Sarwar, G., Pye, H. O. T., Napelenok, S. L., et al. (2013). Evaluation of dust and trace metal estimates from the Community Multiscale Air Quality (CMAQ) model version 5.0. *Geoscientific Model Development*, *6*(4), 883–899. https://doi.org/10.5194/gmd-6-883-2013

Bash, J. O., Cooter, E. J., Dennis, R. W., Walker, J. T., & Pleim, J. E. (2013). Evaluation of a regional air-quality model with bi-directional NH_3 exchange coupled to an agro-ecosystem model. *Biogeosciences*, *10*(3), 1635–1645. https://doi.org/10.5194/bg-10-1635-2013

Bash, J. O., Walker, J. T., Katul, G. G., Jones, M. R., Nemitz, E., & Robarge, W. P. (2010). Estimation of in-canopy ammonia sources and sinks in a fertilized zea mays field. *Environmental Science & Technology*, *44*(5), 1683–1689. https://doi.org/10.1021/es9037269

Bey, I., Jacob, D. J., Yantosca, R. M., Logan, J. A., Field, B. D., Fiore, A. M., et al. (2001). Global modeling of tropospheric chemistry with assimilated meteorology: Model description and evaluation. *Journal of Geophysical Research*, *106*(D19), 23,073–23,095. https://doi.org/10.1029/2001JD000807

Breitburg, D., Levin, L. A., Oschlies, A., Grégoire, M., Chavez, F. P., Conley, D. J., et al. (2018). Declining oxygen in the global ocean and coastal waters. *Science*, *359*(6371), eaam7240. https://doi.org/10.1126/science/aam7240

Byun, D. W., & Schere, K. L. (2006). Review of the governing equations, computational algorithms, and other components of the Models- 3 Community Multiscale Air Quality (CMAQ) Modeling System. *Applied Mechanics Reviews*, *59*(2), 51–77. https://doi.org/10.1115/1.2128636

Campbell, P. C., Bash, J. O., & Spero, T. L. (2019). Updates to the Noah land surface model in WRF-CMAQ to improve simulated meteorology, air quality, and deposition. *Journal of Advances in Modeling Earth Systems*, *11*(1), 231–256. https://doi.org/10.1002/2018MS001422

Chesapeake Bay Foundation (2007). Climate change and the Chesapeake Bay: Challenges, impacts, and the multiple benefits of agricultural conservation work. Retrieved from http://www.cbf.org/document-library/cbf-reports/Climate-Change37bf.pdf

Chesapeake Bay Foundation (2014). The economic benefits of cleaning up the Chesapeake: A valuation of the natural benefits gained by implementing the Chesapeake clean water blueprint. Retrieved from http://www.cbf.org/document-library/cbf-reports/the-economic-benefits-of-cleaning-up-the-chesapeake.pdf

Cooter, E. J., Bash, J. O., Benson, V., & Ran, L.-M. (2012). Linking agricultural management and air-quality models for regional to national-scale nitrogen deposition assessments. *Biogeosciences*, *9*(5), 6095–6127. https://doi.org/10.5194/bgd-9-6095-2012

De Gouw, J. A., Parrish, D. D., Frost, G. J., & Trainer, M. (2014). Reduced emissions of CO_2, NO_x, and SO_2 from U.S. power plants owing to a switch from coal to natural gas with combined cycle technology. *Earth's Future*, *2*(2), 75–82. https://doi.org/10.1002/2013EF000196

Dennis, R. (1997). Using the regional acid deposition model to determine the nitrogen deposition airshed of the Chesapeake Bay Watershed. In J. E. Baker (Ed.), *Atmospheric Deposition of Contaminants to the Great Lakes and Coastal Waters* (pp. 893–1418). Pensacola, Florida: Society of Environmental Toxicology and Chemistry Press.

EPA (2010). Chesapeake Bay total maximum daily load for nitrogen, phosphorus and sediment. U.S. Environmental Protection Agency Chesapeake Bay Program Office. Retrieved from. https://www.epa.gov/sites/production/files/2014-12/documents/cbay_final_tmdl_exec_sum_section_1_through_3_final_0.pdf

EPA (2015). Preparation of emission inventories for the 2011v6.2 emissions modeling platform. Retrieved from https://www.epa.gov/air-emissions-modeling/2011-version-62-technical-support-document

EPA (2016a). Emissions inventory for air quality modeling technical support document: Heavy-duty vehicle greenhouse gas phase 2 final rule. Retrieved from https://nepis.epa.gov/Exe/ZyPDF.cgi/P100PKEE.PDF?Dockey=P100PKEE.PDF

EPA (2016b). Air quality modeling technical support document: Heavy-duty vehicle greenhouse gas phase 2 final rule. Retrieved from https://nepis.epa.gov/Exe/ZyPDF.cgi/P100PKAP.PDF?Dockey=P100PKAP.PDF

EPA (2017). U.S. EPA Office of Research and Development, Community Multiscale Air Quality model version 5.2. Retrieved from https://zenodo.org/record/1167892

EPA (2018). 2014 National Emissions Inventory, version 2. Technical support document. Retrieved from. https://www.epa.gov/sites/production/files/2018-06/documents/nei2014v2_tsd_09may2018.pdf

Eschleman, K. N., & Sabo, R. D. (2016). Declining nitrate-N yields in the Upper Potomac River Basin: What is really driving progress under the Chesapeake Bay restoration? *Atmospheric Environment*, *146*, 280–289. https://doi.org/10.1016/j.atmosenv.2016.07.004

Fisher, A. W., Sanford, L. P., & Suttles, S. E. (2015). Wind stress dynamics in Chesapeake Bay: Spatiotemporal variability and wave dependence in a fetch-limited environment. *Journal of Physical Oceanography*, *45*, 2679–2696. https://doi.org/10.1175/JPO-D-15-0004.1

Foley, K. M., Bash, J. O., Schwede, D., & Pinto, J. (2016). Dynamic evaluation of CMAQ wet deposition estimates: Observed vs modeled trends from 2002–2012. Paper presented at CMAS Conference, Chapel-Hill, NC.

Gao, Y., Fu, J. S., Drake, J. B., Lamarque, J.-F., & Liu, Y. (2013). The impact of emission and climate change on ozone in the United States under representative concentration pathways (RCPs). *Atmospheric Chemistry and Physics*, *13*, 9607–9621. https://doi.org/10.5194/acp-13-9607-2013

Hargreaves, G. H., & Allen, R. G. (2003). History and evaluation of Hargreaves evapotranspiration equation. *Journal of Irrigation and Drainage Engineering*, *129*(1), 53–63. https://doi.org/10.1061/(ASCE)0733-9437(2003)129:1(53)

Henderson, B. H., Akhtar, F., Pye, H. O. T., Napelenok, S. L., & Hutzell, W. T. (2014). A database and tool for boundary conditions for regional air quality modeling: description and evaluation. *Geoscientific Model Development*, *7*, 339–360. https://doi.org/10.5194/gmd-7-339-2014

IPCC (2014). In Core Writing Team, R. K. Pachauri, & L. A. Meyer (Eds.), *Climate change 2014: Synthesis report. Contribution of working groups I, II and III to the fifth assessment report of the Intergovernmental Panel on Climate Change* (p. 151). Geneva, Switzerland: IPCC.

Lam, Y. F., & Fu, J. S. (2009). A novel downscaling technique for the linkage of global and regional air quality modeling. *Atmospheric Chemistry and Physics*, *9*(23), 9169–9185. https://doi.org/10.5194/acp-9-9169-2009

Li, M., Lee, Y. J., Testa, J. M., Li, Y., Ni, W., Kemp, W. M., & Di Toro, D. M. (2016). What drives interannual variability of hypoxia in Chesapeake Bay: Climate forcing versus nutrient loading? *Geophysical Research Letters*, *43*, 2127–2134. https://doi.org/10.1002/2015GL067334

Li, Y., Schichtel, B. A., Walker, J. T., Schwede, D. B., Chen, X., Lehmann, C. M. B., et al. (2016). Increasing importance of deposition of reduced nitrogen in the United States. *Proceedings of the National Academy of Sciences of the United States of America*, *113*(21), 5874–5879. https://doi.org/10.1073/pnas.1525736113

Linker, L. C., Batiuk, R. A., Shenk, G. W., & Cerco, C. F. (2013). Development of the Chesapeake Bay Watershed total maximum daily load allocation. *Journal of the American Water Resources Association*, *49*(5), 986–1006. https://doi.org/10.1111/jawr.12105

Linker, L. C., Dennis, R., Shenk, G. W., Batiuk, R. A., Grimm, J., & Wang, P. (2013). Computing atmospheric nutrient loads to the Chesapeake Bay Watershed and tidal waters. *Journal of the American Water Resources Association*, *49*(5), 1025–1041. https://doi.org/10.1111/jawr.12112

Massad, R.-S., Nemitz, E., & Sutton, M. A. (2010). Review and parameterization of bi-directional ammonia exchange between vegetation and the atmosphere. *Atmospheric Chemistry and Physics*, *10*, 10,359–10,386. https://doi.org/10.5194/acp-10-10359-2010

Mesinger, F., DiMego, G., Kalnay, E., Mitchell, K., Shafran, P. C., Ebisuzaki, W., et al. (2006). North American Regional Reanalysis. *Bulletin of the American Meteorological Society*, *87*(3), 343–360. https://doi.org/10.1175/BAMS-87-3-343

Nazarenko, L., Schmidt, G. A., Miller, R. L., Tausnev, N., Kelley, M., Ruedy, R., et al. (2015). Future climate change under RCP emission scenarios with GISS ModelE2. *Journal of Advances in Modeling Earth Systems*, *7*, 244–267. https://doi.org/10.1002/2014MS000403

Nolte, C. G., Appel, K. W., Kelly, J. T., Bhave, P. V., Fahey, K. M., Collett, J. L. Jr., et al. (2015). Evaluation of the Community Multiscale Air Quality (CMAQ) model Version 5.0 against size-resolved measurements of inorganic particle composition across sites in North America. *Geoscientific Model Development*, *8*(9), 2877–2892. https://doi.org/10.5194/gmd-8-2877-2015

Nolte, C. G., Gilliland, A. B., Hogrefe, C., & Mickley, L. J. (2008). Linking global to regional models to assess future climate impacts on surface ozone levels in the United States. *Journal of Geophysical Research, [Atmospheres]*, *113*, D14307. https://doi.org/10.1029/2007JD008497

Nolte, C. G., Spero, T. L., Bowden, J. H., Mallard, M. S., & Dolwick, P. (2018). The potential effects of climate change on air quality across the CONUS at 2030 under three Representative Concentration Pathways (RCPs). *Atmospheric Chemistry and Physics Discussions*, *18*(20), 15,471–15,489. https://doi.org/10.5194/acp-2018-510

Nowak, J. B., Neuman, J. A., Bahreini, R., Middlebrook, A. M., Holloway, J. S., McKeen, S. A., et al. (2012). Ammonia sources in the California South Coast Air Basin and their impact on ammonium nitrate formation. *Geophysical Research Letters*, *39*, L07804. https://doi.org/10.1029/2012GL051197

Otte, T. L., Nolte, C. G., Otte, M. J., & Bowden, J. H. (2012). Does nudging squelch the extremes in regional climate modeling? *Journal of Climate*, *25*, 7046–7066. https://doi.org/10.1175/JCLI-D-12-00048.1

Otte, T. L., & Pleim, J. E. (2010). The Meteorology-Chemistry Interface Processor (MCIP) for the CMAQ modeling system: Updates through MCIPv3.4.1. *Geoscientific Model Development*, *3*, 243–256. https://doi.org/10.5194/gmd-3-243-2010

Paerl, H. W., Dennis, R. L., & Whitall, D. R. (2002). Atmospheric deposition of nitrogen: Implications for nutrient over-enrichment of coastal waters. *Estuaries*, *25*(4), 677–693. https://doi.org/10.1007/BF02804899

Paulot, F., Jacob, D. J., Pinder, R. W., Bash, J. O., Travis, K., & Henze, D. K. (2014). Ammonia emissions in the United States, European Union, and China derived by high-resolution inversion of ammonium wet deposition data: Interpretation with a new agricultural emissions inventory (MASAGE_NH3). *Journal of Geophysical Research: Atmospheres*, *119*, 4343–4364. https://doi.org/10.1002/2013JD021130

Powers, J. G., Klemp, J. B., Skamarock, W. C., Davis, C. A., Dudhia, J., Gill, D. O., et al. (2017). The Weather Research and Forecasting model: Overview, system efforts, and future directions. *Bulletin of the American Meteorological Society*, *98*(8), 1717–1737. https://doi.org/10.1175/BAMS-D-15-00308.1

Reis, S., Pinder, R. W., Zhang, M., Lijie, G., & Sutton, M. (2009). Reactive nitrogen in atmospheric emission inventories. *Atmospheric Chemistry and Physics*, *9*(19), 7657–7677. https://doi.org/10.5194/acpd-9-12413-2009

Saha, S., Moorhi, S., Pan, H.-L., Wu, X., Wang, J., Nadiga, S., et al. (2010). The NCEP Climate Forecast System Reanalysis. *Bulletin of the American Meteorological Society*, *91*(8), 1015–1058. https://doi.org/10.1175/2010BAMS3001.1

Sarwar, G., Appel, K. W., Carlton, A. G., Mathur, R., Schere, K., Zhang, R., & Majeed, M. A. (2011). Impact of a new condensed toluene mechanism on air quality model predictions in the US. *Geoscientific Model Development*, *4*, 183–193. https://doi.org/10.5194/gmd-4-183-2011

Scully, M. E. (2010). The importance of climate variability to wind driven modulation of hypoxia in the Chesapeake Bay. *Journal of Physical Oceanography*, *40*, 1435–1440. https://doi.org/10.1175/2010JPO4321.1

Separovic, L., Alexandru, A., Laprise, R., Martynov, A., Sushama, L., Winger, K., et al. (2013). Present climate and climate change over North America as simulated by the fifth-generation Canadian regional climate model. *Climate Dynamics*, *41*(11-12), 3167–3201. https://doi.org/10.1007/s00382-013-1737-5

Seltzer, K., Chris, N., Spero, T., Appel, W., & Xing, J. (2016). Evaluation of near surface ozone and particulate matter in air quality simulations driven by dynamically downscaled historical meteorological fields. *Atmospheric Environment*, *138*, 42–54.

Shenk, G. W., & Linker, L. C. (2013). Development and application of the 2010 Chesapeake Bay Watershed total maximum daily load model. *Journal of the American Water Resources Association*, *49*(5), 1042–1056. https://doi.org/10.1111/jawr.12109

Simon, H., & Bhave, P. V. (2012). Simulating the degree of oxidation in atmospheric organic particles. *Environmental Science & Technology*, *46*(1), 331–339. https://doi.org/10.1021/es202361w

Skamarock, W. C., & Klemp, J. B. (2008). A time-split nonhydrostatic atmospheric model for weather research and forecasting applications. *Journal of Computational Physics*, *227*, 3465–3485. https://doi.org/10.1016/j.jcp.2007.01.037

Spero, T. L., Nolte, C. G., Bowden, J. H., Mallard, M. S., & Herwehe, J. A. (2016). The impact of incongruous lake temperatures on regional climate extremes downscaled from the CMIP5 archive using the WRF model. *Journal of Climate*, *29*, 839–853. https://doi.org/10.1175/JCLI-D-15-0233.1

Sutton, M. A., Reis, S., Riddick, S. N., Dragosits, U., Nemitz, E., Theobald, M. R., et al. (2013). Toward a climate dependent paradigm of ammonia emission and deposition. *Philosophical Transactions of the Royal Society B*, *368*(1621), 20130166. https://doi.org/10.1098/rstb.2013.0166

Thomson, A. M., Calvin, K. V., Smith, S. J., Kyle, G. P., Volke, A., Patel, P., et al. (2011). RCP4.5: A pathway for stabilization of radiative forcing by 2100. *Climatic Change*, *109*(1-2), 77–94. https://doi.org/10.1007/s10584-011-0151-4

Trail, M., Tsimpidi, A. P., Liu, P., Tsigaridis, K., Hu, Y., Nenes, A., & Russell, A. G. (2013). Downscaling a global climate model to simulate climate change over the US and the implication on regional and urban air quality. *Geoscientific Model Development*, *6*(5), 1429–1445. https://doi.org/10.5194/gmd-6-1429-2013

van Vuuren, D. P., Edmonds, J., Kainuma, M., Riahi, K., Thomson, A., Hibbard, K., et al. (2011). The representative concentration pathways: an overview. *Climatic Change*, *109*(1-2), 5–31. https://doi.org/10.1007/s10584-011-0148-z

Walker, J. M., Philip, S., Martin, R. V., & Seinfeld, J. H. (2012). Simulation of nitrate, sulfate, and ammonium aerosols over the United States. *Atmospheric Chemistry and Physics*, *12*(22), 11,213–11,227. https://doi.org/10.5194/acp-12-11213-2012

Wang, J., & Kotamarthi, V. R. (2015). High-resolution dynamically downscaled projections of precipitation in the mid and late 21st century over North America. *Earth's Future*, *3*, 268–288. https://doi.org/10.1002/2015EF000304

Warner, J. X., Dickerson, R. R., Wei, Z., Strow, L. L., Wang, Y., & Liang, Q. (2017). Increased atmospheric ammonia overthe world's major agricultural areas detected from space. *Geophysical Research Letters*, *44*, 2875–2884. https://doi.org/10.1002/2016GL072305

Weaver, C. P., Liang, X.-Z., Zhu, J., Adams, P. J., Amar, P., Avise, J., et al. (2009). A preliminary synthesis of modeled climate change impacts on US regional ozone concentrations. *Bulletin of the American Meteorological Society*, *90*(12), 1843–1864. https://doi.org/10.1175/2009BAMS2568.1

Yahya, K., Campbell, P., & Zhang, Y. (2017). Decadal application of WRF/Chem for regional air quality and climate modeling over the U.S. under the representative concentration pathways scenarios. Part 2: Current vs. future simulations. *Atmospheric Environment*, *152*, 584–604. https://doi.org/10.1016/j.atmosenv.2016.12.028

Zhang, Y., Foley, K. M., Schwede, D. B., Bash, J. O., Pinto, J. P., & Dennis, R. L. (2019). A measurement-model fusion approach for improved wet deposition maps and trends. *Journal of Geophysical Research: Atmospheres*, *124*, 4237–4251. https://doi.org/10.1029/2018JD029051

Zhu, L., Henze, D. K., Cady-Pereira, K. E., Shephard, M. W., Luo, M., Pinder, R. W., et al. (2013). Constraining U.S. ammonia emissions using TES remote sensing observations and the GEOS-Chem adjoint model. *Journal of Geophysical Research: Atmospheres*, *118*, 3355–3368. https://doi.org/10.1002/jgrd.50166